Plasmonic metagratings for simultaneous determination of Stokes parameters

Pors, Anders Lambertus; Nielsen, Michael Grøndahl; Bozhevolnyi, Sergey I.

Plasmonic channel waveguides in random arrays of metallic nanoparticles

EDUARDO PISANO,[1] VICTOR COELLO,[2,*] CESAR E. GARCIA-ORTIZ,[2,3]
YITING CHEN,[4] JONAS BEERMANN,[4] AND SERGEY I. BOZHEVOLNYI[4]

[1]*División de Física Aplicada, Centro de Investigación Científica y de Educación Superior de Ensenada, Carretera Ensenada-Tijuana No. 3918, Ensenada, BC 22860, Mexico*
[2] *Unidad Monterrey, Centro de Investigación Científica y de Educación Superior de Ensenada, Alianza Centro 504, Apodaca, NL, 66629, Mexico*
[3] *CONACYT – CICESE, Unidad Monterrey, Alianza Centro 504, Apodaca, NL, 66629, Mexico*
[4]*Centre for Nano Optics, University of Southern Denmark, Campusvej 55, DK-5230 Odense M, Denmark*
*vcoello@cicese.mx

Abstract: We report detailed characterization of surface plasmon-polariton guiding along 1-, 1.5- and 2-μm-wide channels in high-density (~75 μm^{-2}) random arrays of gold 70-nm-high and 50-nm-wide nanoparticles fabricated on a 70-nm-thin gold film supported by a 170-μm-thick silica substrate. The mode propagation losses, effective index dispersion, and scattering parameters are characterized using leakage-radiation microscopy, in direct and Fourier planes, in the wavelength range of 740–840 nm. It is found that the mode supported by 2-μm-wide channels propagates over > 10 μm in straight waveguides, with the corresponding S-bends and Y-splitters functioning reasonably well. The results show that the SPP waves can efficiently be guided by narrow scattering-free channels cut through randomly corrugated surface regions. The potential of this waveguiding mechanism is yet to be fully explored by tuning the scattering mean-free path and localization length via the density and size of random nanoparticles. Nevertheless, the results obtained are encouraging and promising diverse applications of these waveguide components in plasmonic circuitry.

References and links

1. S. Maier, *Plasmonics: Fundamentals and Applications* (Springer, 2007).
2. Z. Han and S. I. Bozhevolnyi, "Radiation guiding with surface plasmon polaritons," Rep. Prog. Phys. **76**(1), 016402 (2013).
3. Y. Fang and M. Sun, "Nanoplasmonic waveguides: towards applications in integrated nanophotonic circuits," Light Sci. Appl. **2**, e66 (2013).
4. A. Krasavin and A. Zayats, "Active nanophotonic circuitry based on dielectric-loaded plasmonic waveguides," Adv. Opt. Mater. **3**(12), 1662–1690 (2015).
5. I. De Leon and P. Berini, "Amplification of long-range surface plasmons by a dipolar gain medium," Nat. Photonics **4**(6), 382–387 (2010).
6. C. Garcia, V. Coello, Z. Han, I. P. Radko, and S. I. Bozhevolnyi, "Partial loss compensation in dielectric-loaded plasmonic waveguides at near infra-red wavelengths," Opt. Express **20**(7), 7771–7776 (2012).
7. C. Garcia, V. Coello, Z. Han, I. P. Radko, and S. I. Bozhevolnyi, "Experimental characterization of dielectric-loaded plasmonic waveguide-racetrack resonators at near-infrared wavelengths," Appl. Phys. B **107**(2), 401–407 (2012).
8. Y. Ma, G. Farrell, Y. Semenova, H. P. Chan, H. Zhang, and Q. Wu, "Novel dielectric-loaded plasmonic waveguide for tight-confined hybrid plasmon mode," Plasmonics **8**(2), 1259–1263 (2013).
9. R. Oulton, V. Sorger, D. A. Genov, D. Pile, and X. Zhang, "A hybrid plasmonic waveguide for subwavelength confinement and long-range propagation," Nat. Photonics **2**(8), 496–500 (2008).
10. S. I. Bozhevolnyi and V. Coello, "Elastic scattering of surface plasmon polaritons modeling and experiment," Phys. Rev. B **58**(16), 10899–10910 (1998).
11. M. I. Stockman, S. V. Faleev, and D. J. Bergman, "Localization versus delocalization of surface plasmons in nanosystems: Can one state have both characteristics?" Phys. Rev. Lett. **87**(16), 167401 (2001).
12. V. Coello, R. Cortes, C. Garcia-Ortiz, and N. Elizondo, "Surface plasmon excitation and manipulation in disordered two dimensional nanoparticle arrays," Nano **8**(4), 44–55 (2013).

13. S. I. Bozhevolnyi, "Localization phenomena in elastic surface plasmon polariton scattering," Phys. Rev. B **54**(11), 8177 (1996).
14. V. Coello, "Surface plasmon polariton localization," Surf. Rev. Lett. **15**(6), 867–880 (2008).
15. X. Shi, X. Chen, B. Malomed, N. Panoiu, and F. Ye, "Anderson localization at the subwavelength scale and loss compensation for surface-plasmon polaritons in disordered arrays of metallic nanowires," Phys. Rev. B **89**(19), 195428 (2014).
16. S. I. Bozhevolnyi, V. S. Volkov, and K. Leosson, "Localization and waveguiding of surface plasmon polaritons in random nanostructures," Phys. Rev. Lett. **89**(18), 186801 (2002).
17. S. I. Bozhevolnyi, V. Volkov, K. Leosson, and A. Boltasseva, "Surface plasmon waveguiding in random nanostructures," J. Micr. **209**(3), 209–213 (2002).
18. S. I. Bozhevolnyi, J. Erland, K. Leosson, P. M. Skovgaard, and J. M. Hvam, "Waveguiding in surface plasmon polariton band gap structures," Phys. Rev. Lett. **86**(14), 3008–3011 (2001).
19. S. F. Liew, S. M. Popoff, A. P. Mosk, W. L. Vos, and H. Cao, "Transmission channels for light in absorbing random media: From diffusive to ballistic-like transport," Phys. Rev. B **89**(22), 224202 (2014).

1. Introduction

Plasmonic nanostructures have the potential to combine the very large bandwidth of photonics and the subwavelength confinement of surface plasmon polaritons (SPPs) [1]. This could lead to a new generation of nanoscale optical integrated circuits. In this context, SPP-based (plasmonic) waveguides constitute one of the key elements for realizing this down-scaling technology, and the progress in SPP-based nanophotonics has been reviewed in a number of papers [2–4]. In general, plasmonic waveguides exhibit a fundamental trade-off between subwavelength confinement and propagation loss. In other words, increasing the mode confinement is associated with a decrease in the mode propagation length. In order to optimize this trade-off, several configurations have been proposed and evaluated including the use of gain media as a mechanism to compensate ohmic loss [5, 6], conventional and novel designs, e.g. dielectric-loaded plasmonic waveguides [7, 8], and hybrid plasmonic waveguides [9]. However, since the loss compensation in propagating SPPs is far from being a trivial problem, the search for novel plasmonic waveguide configurations that might be better (than already developed ones) suited for particular applications is going on. Typically, the design of waveguides is based on periodic or individual surface nanostructures, whereas less attention has been paid to disordered nanostructures, since disorder is usually not reproducible. However, the fabrication of periodic nanostructures requires a high degree of control and precision, in order to ensure that the structures behave as designed, and common lithography methods cannot easily reach the required resolution. Regarding the SPP interaction with two-dimensional random nanoparticles arrays, theoretical and experimental studies have been conducted [10–12]. The size scale where this interaction occurs is of utmost importance for understanding electromagnetic enhancement mechanisms such as strong (Anderson) localization of SPP waves [13–15]. Of particular interest, in this context, is the study of the inhibition of SPP penetration into randomly corrugated surface regions and SPP guiding along random-nanoparticle plasmonic channel waveguides (RN-PCWs) in these regions [16, 17]. The effect is similar to that of the photonic band gap in periodically located scatterers [18] and has been characterized by using near-field imaging with a scanning near field optical microscopy and an arrangement for SPP excitation in the Kretschmann configuration with a (practically) plane-wave incidence [16, 17], i.e., with a global (rather than local) SPP excitation. This experimental configuration is clearly of limited use, since guided SPP modes overlap spatially with locally excited ones (in the waveguide channels) so that even basic mode characteristics, such as the mode propagation length, become cumbersome to evaluate.

A proper way to overcome this limitation is to employ a local SPP excitation forming an SPP beam, which is incident on the structure of interest and coupled thereby to the RN-PCW mode. In this work, local SPP excitation along with convenient leakage-radiation mapping of SPP propagation [7] is employed, thereby allowing us to report, for the first time to our knowledge, direct evaluation of the SPP propagation losses and other waveguide mode

characteristics for straight waveguides based on random arrays of metallic nanoparticles, as well as performance of the corresponding S-bends and Y-splitters.

2. Materials and methods

All plasmonic nanostructures are fabricated by using standard electron-beam lithography (EBL) and lift-off patterning. The process is as follows: first, a 70-nm-thick gold film is deposited on a 0.17-mm-thick silica substrate. Second, the sample is spin-coated with poly-methyl-methacrylate (PMMA), which acts as a positive resist. Then, the sample is patterned using the EBL module for subsequent development. At this point, a second evaporation process is performed to generate the structures with gold. Finally, a solvent (generally acetone) is used to dissolve the remaining resist and complete the lift-off. The thickness of the gold thin film is set to 70 nm because, for smaller thicknesses, the propagation length starts to decrease. The straight waveguides [Fig. 1(a)] consist of corrugation-free channels of different widths (w = 1, 1.5 and 2 μm) in high density (designed to $n \sim 75$ μm^{-2}) scattering regions composed of gold 70-nm-high and 50-nm-wide bumps randomly distributed over designed areas on the gold film [Fig. 1(b)]. The fabricated S-bends structures are composed of two bends connecting two parallel channel waveguides with an offset d_0 with respect to each other. The Y-splitters are composed of two mirrored S-bends [Figs. 1(d) and 1(e)]. The design of the bends follows a path given by

$$d(x) = \frac{d_0}{2\pi}\left[\frac{2\pi x}{\Lambda} - \sin\left(\frac{2\pi x}{\Lambda}\right)\right], \tag{1}$$

where Λ is the length of the bend. The input of all the waveguides is made in the form of a funnel, with a starting width f_w = 5 μm, in order to achieve an efficient coupling to the SPP guided mode. The performance of the fabricated components is characterized using leakage-radiation microscopy (LRM) with a tunable (740–840 nm) Ti:Sapphire laser as a source [7].
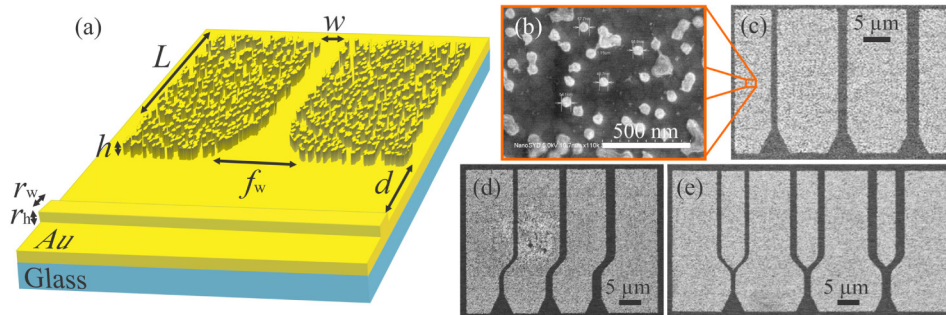

Fig. 1. (a) Schematic design of the straight RN-PCWs. (b) Scanning electron microscopy (SEM) image showing the fabricated scatterers inside the random structure. SEM images of (c) straight channel waveguides, (d) waveguides with S-bends, and (e) Y-splitting channel waveguides of different widths of 1, 1.5 and 2 μm, respectively.

In contrast with previous experiments [16, 17], here the propagating gold/air SPP mode is locally excited, by using a straight gold ridge with the width r_w = 200 nm, and directly coupled into the waveguide structures. The ridge is placed at the distance d = 5 μm away from the waveguides inputs in order to facilitate the SPP excitation [Fig. 1(a)].

3. Results and discussion

3.1 Localization length and scattering parameters

Strong localization of SPPs is necessary to achieve the inhibition of SPP propagation inside the corrugated areas and thereby guarantee the confinement of the guided mode along the

corrugation-free channels [16]. Since two-dimensional waves can be strongly localized with any degree of disorder (in the absence of dissipation), the only condition for the strong SPP localization is that the SPP propagation length should be much larger than the SPP scattering mean-free path ($L_{SP} \gg l$) [16]. Note that, in practice, this implies that, due to the exponential divergence of the localization length with the scattering mean-free path, the latter should be similar to or smaller than the SPP wavelength ($l \lesssim \lambda_{SP}$). The propagation length L_{SP} is experimentally found to vary between 23 and 26 µm in the wavelength range 740–840 nm. In order to estimate the scattering mean free path l, we use the expression $\xi \sim l \cdot \exp(2\pi l/\lambda)$, where ξ is the localization length, which can be related to the penetration depth of the metal-air SPP into the corrugated area. In addition, we assume that the SPP intensity attenuation inside the corrugation is exponential: $I(x) = I_0 \cdot \exp(-2x/\xi)$, where x is the propagation distance into the corrugation. The localization length is estimated by directing the SPP beam onto the rectangular area filled randomly with nanoparticles and assessing the intensity decay of the SPP beam inside the corrugation using the LRM imaging [Fig. 2]. The procedure consists of mapping the profiles of the intensity distribution along the propagation direction inside the corrugated region [Figs. 2(c)–2(f)], to find ξ through numerical fitting.
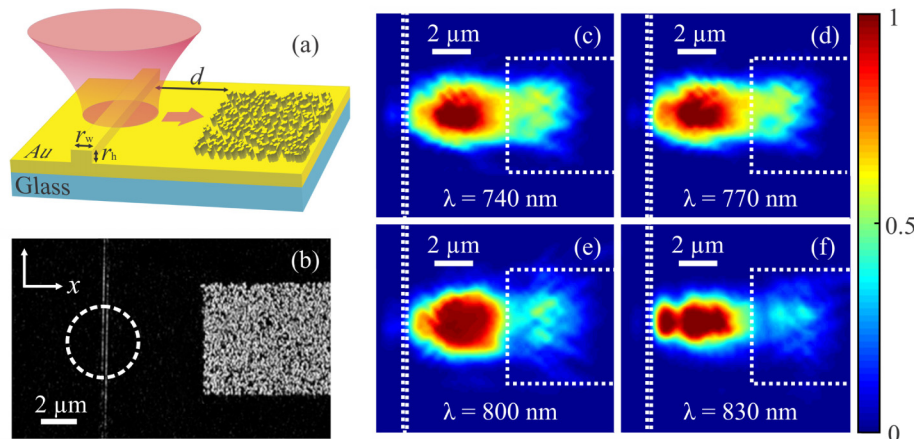

Fig. 2. (a) Schematic showing the SPP beam excited from the ridge impinging directly into the random structure. (b) SEM image of the ridge used for coupling (vertical line in the left) and the random structure (right). The dotted circle represents the position at which the laser is focused to launch the SPPs. (c)–(f) LRM images of the intensity distribution of the SPP entering the corrugated area at a wavelength of (c) 740, (d) 770, (e) 800, and (f) 830 nm. The excitation spot and the left propagating beam are filtered out with spatial filters. The dotted vertical line depicts the position of the excitation ridge, and the dotted rectangle is the area containing the randomly placed nanoparticles.

The SPP beam is excited at the metallic ridge and travels 5 µm (gradually diverging) before entering the random structure. Once inside the random array, the beam first propagates over ~2 µm seemingly without strong attenuation, and then undergoes a rapid decay and complete damping over the next 2 µm [Figs. 2(c)–2(f)]. The existence of the transition region is probably related to the circumstance that the strongly localized states can be formed only inside random structures (to be sufficiently far away from their boundaries). The intensity of the SPP beam outside of the corrugated area does not show interference fringes, signs of Bragg reflection, which indicates that the energy is dissipated inside the random structure by means of multiple SPP scattering and eventual absorption. Previous works have shown experimentally that the SPP waves are mostly scattered elastically (in the plane) by similarly sized nanoparticles [17]. The intensity profile of the beam entering the corrugated region is averaged across 2 µm in the transverse direction of the beam to obtain a smooth curve for further determination of the localization length ξ. The intensity profiles show a quasi-steady

signal in the first 2 μm after entering the structure, and a rapid decay afterwards [Fig. 3(a)]. In order to determine ξ, and due to the irregular (non-exponential) form of the curves, we decided to consider the values of intensity profile after the beam had traveled ~2.8 μm inside the random structure, i.e. when the signal starts to actually decay (black vertical line in Fig. 3(a)). Even then, the profiles do not follow an exponential decay ($R^2 < 0.7$) but the obtained fit for ξ gives a reasonable estimate of the attenuation caused by the structure. The obtained values of ξ vary slightly from 1 to 2 μm, increasing slowly with the wavelength, with two peaks at 750 and 830 nm, which might be associated with accidental excitation of (close to) preferred eigenchannels [19]. The scattering mean free path l is obtained for every wavelength by solving the transcendental equation $\exp(2\pi l/\lambda) - \xi/l = 0$. The value range for l is found to be from 200 to almost 300 nm, which is considerably smaller than the SPP wavelength, and the ratio of L_{SP} to l is ~100, an indication that the SPP waves are strongly localized in these random areas.
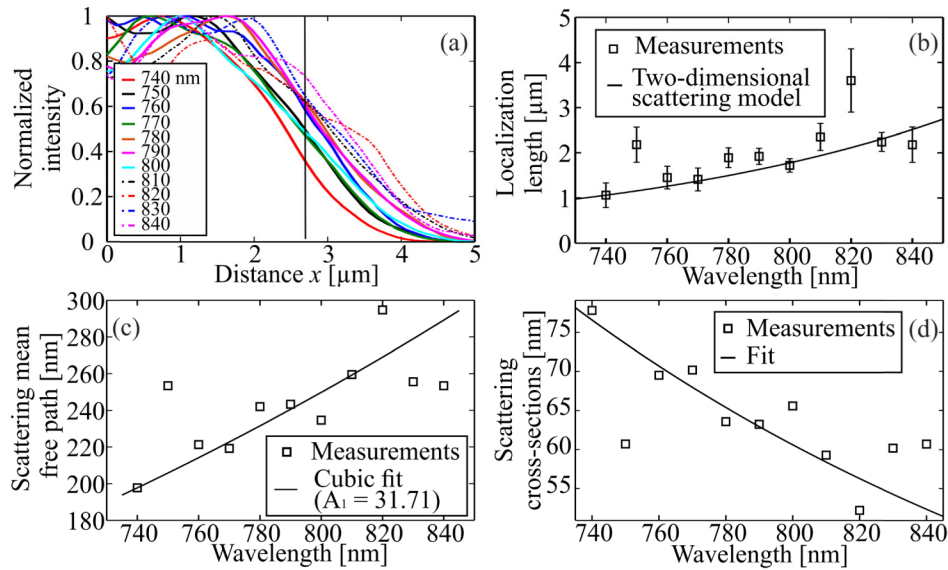

Fig. 3. (a) Averaged intensity profiles along the propagation direction of the SPP beam entering the corrugated area for wavelengths in the range 740–840 nm. (b) Localization lengths obtained from the exponential fit and the two-dimensional scattering model. (c) Scattering mean-free path and (d) scattering cross sections.

The scattering cross-section is estimated by using the obtained values of l in the long-wavelength approximation [17]: $\sigma \sim (nl)^{-1} \sim \lambda^{-3}$. Only a constant multiplicative factor is left as a fitting parameter yielding a value $A_1 = 31.71$ [Fig. 3(c)]. Despite noticeable deviations, it is clear that the values of σ follow the expected trend [Fig. 3(d)]. It is very interesting to note that $\sigma \sim 70$ nm at short wavelengths (~760 nm) coincides with the height of the fabricated nanoparticles. Moreover, the magnitude of σ at $\lambda = 740$ nm is 35% larger than that at 840 nm. The fact, that the scattering cross-section decreases when increasing the wavelength, suggests that the best performance of the fabricated SPP waveguides should be expected to find at shorter wavelengths, due to stronger localization effects.

3.2 Straight RN-PCWs

Straight RN-PCWs are characterized using the LRM in both the image and frequency plane. The intensity distribution observed in the image plane showed well-defined SPP excitation with the excited SPP wave impinging into the funnel region [Fig. 4(a)], where it couples successfully into the RN-PCW mode. The RN-PCW mode in the straight waveguide

propagates efficiently along the channel, although there is a strong decrease of the mode propagation length L_{CW} [Fig. 4(c)] as compared to the free propagating SPP (L_{SP} ~24 μm) mainly due to the absorption and scattering in the corrugated zone. The intensity profile along the propagation direction of the RN-PCW mode follows an exponential decay, which allows for a direct determination of the propagation length of the mode [Fig. 4(b)]. The propagation length of the three straight waveguides of different widths, $w = 1$, 1.5 and 2 μm, is characterized in the wavelength range of 740–840 nm [Fig. 4(c)]. The straight RN-PCWs show a decrease in the propagation length, as the wavelength increases, opposite to the common increment observed in other types of plasmonic waveguides [6,7]. The reason is associated with decreased localization strength and scattering cross-section at longer wavelengths, which means more penetration into and dissipation in the corrugated areas on both sides of the channel. However, this effect appeared only in the waveguides of widths $w =$ 2 and 1.5 μm. The narrowest waveguide, $w = 1$ μm, showed a steady, even increasing, value of the propagation length [Fig. 4(c)]. This effect, although seems contrary to the first two, is a consequence of the same phenomenon.
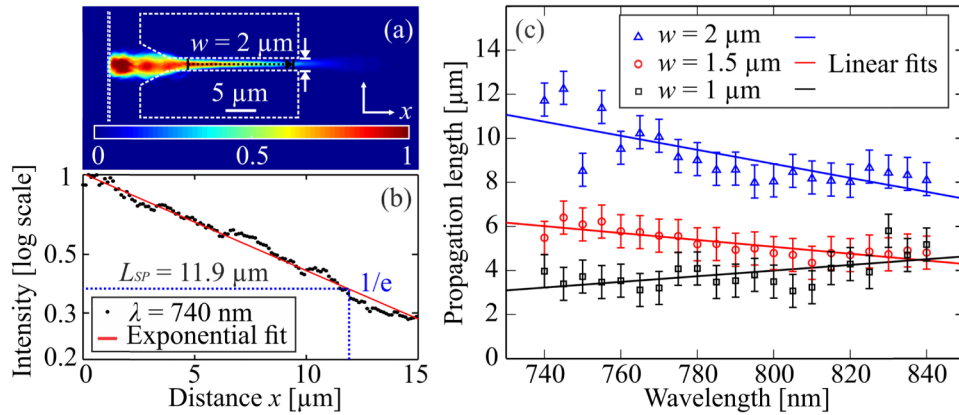

Fig. 4. (a) LRM image of the intensity distribution of the RN-PCW mode propagating from left to right, at an excitation wavelength of 740 nm. The dotted lines represent the boundary of the random structure and the ridge used for excitation. The excitation spot and the left propagating beam are blocked to ease visualization. (b) Averaged intensity profile of the RN-PCW mode along the propagation direction x (black dotted arrow in (a)). (c) Propagation length for the three waveguide widths in the wavelength range 740–840 nm.
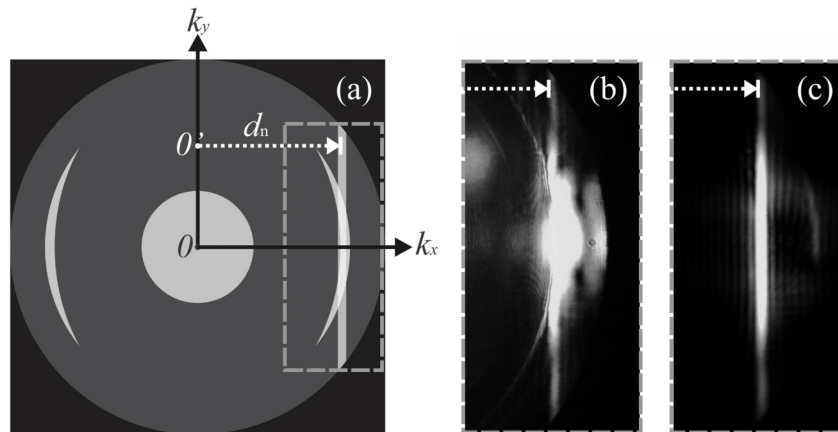

Fig. 5. (a) Fourier plane schematic. The inner gray circle corresponds to the numerical aperture (NA) of the focusing objective (0.40), while the outermost corresponds to the NA of the

collection objective (1.25). The two lateral crescents correspond to the free-propagating SPP excited in the ridge. The clear vertical line to the right is a signature of a guided mode. (b) Experimental LRM image showing a section of the Fourier plane, corresponding to the area contained inside the dashed rectangle in (a). (c) Filtered image of (b).

The waveguide is too narrow to support the RN-PCW mode effectively. This can be deduced from the small values of the propagation length (~3 μm). In this case, an increase of the penetration into the structure, especially at the sides of the funnel, and subsequently leaking into the channel over the next few μm, can result in an increment of the intensity along the channel. The signature of a guided mode can be observed in the spatial frequency domain which is accessible in the Fourier plane of the LRM [Fig. 5]. The LRM image contains a clearly visible straight vertical line (along the k_y axis), which is associated with a guided mode propagating in the x-direction [Fig. 5(b)]. Such evidence reinforces our results, showing that the multiple scattering of SPPs couples into channel modes with a well-defined wave-vector κ_x. Our LRM imaging system allows for spatial filtering in the Fourier plane to obtain better images in the image plane.
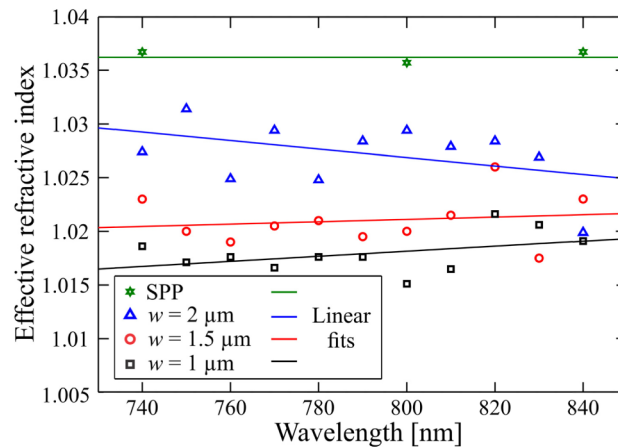

Fig. 6. Effective refractive index as a function of wavelength of the RN-PCW mode for the three different waveguides. Linear fits are included as a guide. The green stars and line correspond to the effective index n_{eff} of free SPP wave at the gold-air interface.

One can employ the same reasoning, but in an inverse manner, in order to obtain better (more specific) images in the Fourier plane by placing spatial filters in the image plane. The motivation is to filter out the contributions from the free-propagating (outside the random structure) SPPs, which have almost the same effective refractive index n_{eff}, and overlap in the Fourier plane [Figs. 5(b) and 5(c)]. Using this technique, we measured the n_{eff} for the three different waveguides in the same wavelength range as before [Fig. 6]. The effective refractive index decreases for smaller channel widths, causing an increase of the guided mode wavelength λ_G, a trend that is similar to that found with dielectric waveguides. Thus, the wavelengths of the RN-PCW modes determined at the excitation wavelength $\lambda_0 = 740$ nm yield the following values: $\lambda_G = 718$, 725 and 728 nm for the waveguide widths $w = 2$, 1.5 and 1 μm, respectively. A linear fit of the experimental values of the effective index showed a rather weak dependence on the wavelength [Fig. 6]. However, one should consider that the uncertainty of the measurement of n_{eff} associated with the limited amount of pixels is ~0.005. From this result we can only conclude that n_{eff} do not vary more than 0.01 in the wavelength range of 740–840 nm.

3.3 RN-PCW S-bends and Y-splitters

S-bend and Y-splitter channels in the random structure are characterized by measuring the transmission efficiency and determining the inherent (i.e., on the top of the propagation loss

found in straight waveguides) loss. The excitation of the beam is the same as in the previous section, and the same three different channel widths are characterized. The methodology used to measure the transmission consists in taking an averaged cross-section at a specific point A before the bend or splitter. The profile is integrated to obtain a value of the intensity in that point. The output intensity is measured in the same way at point B [Fig. 7(a)]. The length t of the trajectory from A to B is chosen to be 6 μm (point A was 2 μm before the bend, while point B is set 2 μm after the end of the bend). In the case of the Y-splitters, there are two outputs, namely B_1 and B_2, defined in a similar way [Fig. 8(a)].
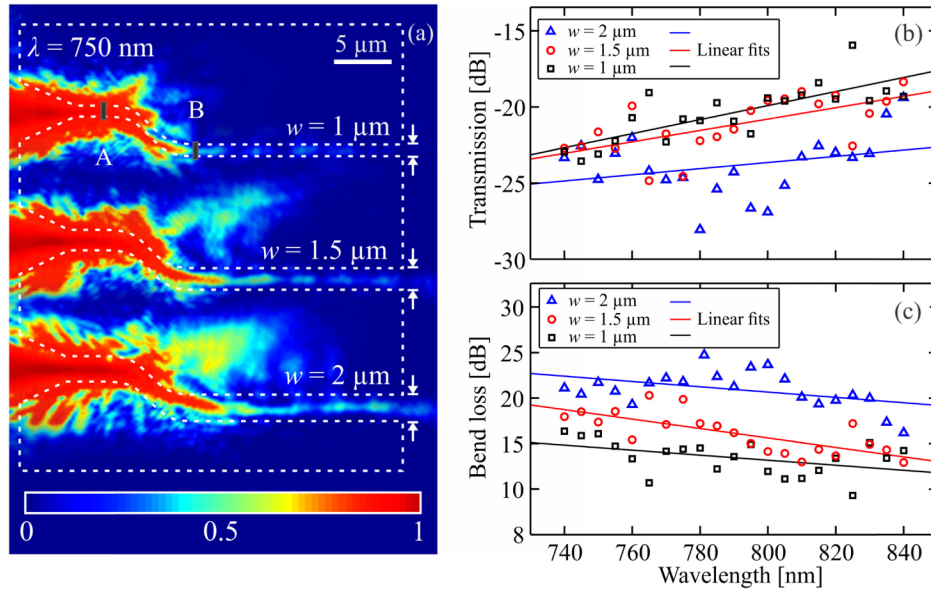

Fig. 7. (a) LRM image of the intensity distribution of three waveguides of different widths with S-bends at an excitation wavelength of 750 nm. (b) Transmission and (c) bend loss of the S-bend of the three structures in the wavelength range of 740–840 nm.

For the S-bends, we consider that the transmission from A to B is found from the relation $T = I(B)/I(A)$ [Fig. 7(b)]. The transmission measurements show an increase of the signal as the excitation wavelength increases, with the best efficiency for the narrowest waveguide. The LRM images show how the guided mode leaks into the random structure for the waveguides of $w = 1.5$ and 2 μm, causing a decrease in transmission. The losses, which occur in the bend, are mainly due to the bend losses $\sigma_S(\lambda)$, which account for the leaking and out-of-plane scattering, as well as from the propagation loss of the mode. The losses are calculated by assuming that $I(B) = I_0 \cdot \exp(-t/L_{CW}) \, \sigma_S(\lambda)$, where $I_0 = I(A)$, and $\sigma_S(\lambda)$ are derived from the experimental values [Fig. 7(c)]. The Y-splitters are characterized using a similar procedure [Fig. 8(a)]. The Y-splitter is designed to act as a 50-50 beam splitter of the RN-PCW mode. The mode arrives to a bifurcation point where the mode is expected to split and propagate along the other two channels. In this case, the transmission is measured with the relation $T = [I(B_1) + I(B_2)]/I(A)$. Similarly to the S-bends, the transmitted signal increases with the wavelength [Fig. 8(b)]. Compared to the S-bends, the efficiency of the Y-splitter is much better ($T \sim 10$ dB), mainly for the reason that the extra channel captures the strong leakage observed in the bends. In the waveguide of $w = 1$ μm, the RN-PCW mode is efficiently guided and split, while for the wider channels, the mode starts to leak at the bifurcation point [Fig. 8(a)]. The losses are calculated using the expression $[I(B_1) + I(B_2)] = I_0 \cdot \exp(-t/L_{CW}) \, \sigma_Y(\lambda)$, where $I_0 = I(A)$ and $\sigma_Y(\lambda)$ is the Y-split loss, and are considerably lower compared to the S-bends [Fig. 8(c)]. There are cases where the losses are very close to 0 dB. A similar trend observed in the S-bends is present in the Y-splitters: the losses decrease with increasing

wavelength, except for the $w = 1$ μm case. It is important to note that the coupling efficiency into the waveguide is better for the wider structures, as it can be seen from the intensity distribution in Fig. 8(a) that a large fraction of the energy is lost in the input channel of the narrowest waveguides.
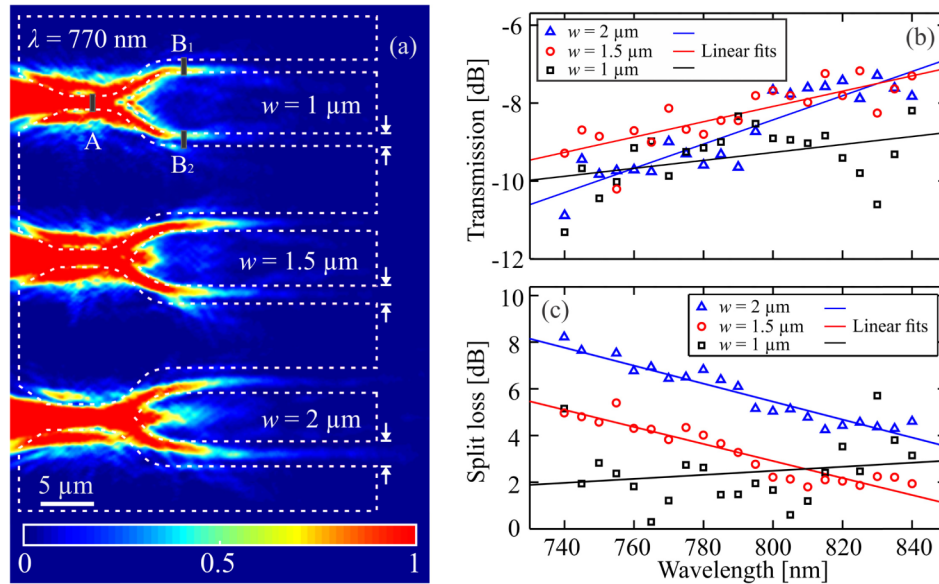

Fig. 8. (a) LRM image of the intensity distribution of three waveguides of different widths with Y-splitters at an excitation wavelength of 770 nm. (b) Transmission and (c) Y-splitter losses of the three structures in the wavelength range of 740–840 nm.

The performance of the Y-splitter is also characterized by analyzing averaged intensity cross-sections along the transverse direction of the Y-splitter, through points B_1 and B_2 [Figs. 9(a)–9(c)]. The Y-splitters showed a good 50-50 performance in almost all the cases, with certain combinations of width and wavelength, such as $w = 2$ μm and $\lambda = 740$ nm, and $w = 2$ μm and $\lambda = 800$ nm, producing the best results. At longer wavelengths the mode fails to follow the channel and leaks into the random structure [Fig. 9(c)]. One can speculate on whether the design used for S-bends and Y-splitters, while being well suitable for conventional dielectric and plasmonic waveguides, should be modified considerably when employing channels in random structures, e.g., by introducing gradients in the density of randomly placed nanoparticles in the corresponding regions.
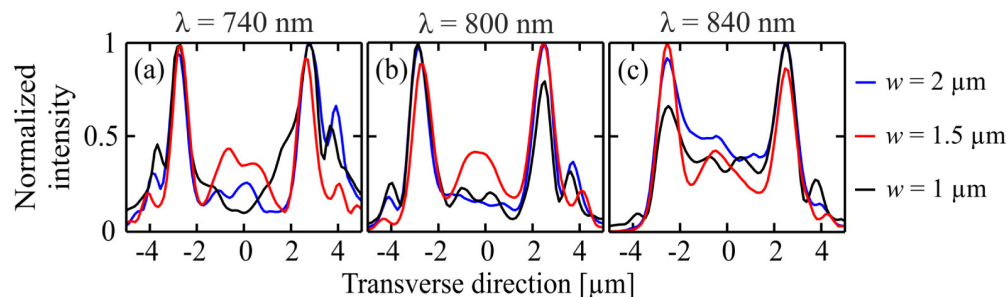

Fig. 9. Averaged intensity cross-sections along the transverse direction of the Y-splitter through points B_1 and B_2 for the three different channel widths at an excitation wavelength of (a) 740 nm, (b) 800 nm, and (c) 840 nm.

4. Conclusions

In this work, we have reported detailed characterization of SPP guiding along channels in dense arrays of randomly distributed nanoparticles, i.e., by RN-PCWs. In contrast with previous approaches [16], we report a clear evidence of the excitation and propagation of RN-PCW modes formed due to multiple SPP scattering and strong localization. Moreover, the characterization using the LRM was decisive in this matter, since the signature of the guided mode appeared clearly in the spatial frequency domain. The scattering parameters were also characterized with this technique, confirming the strong localization of SPPs inside the random structures and good agreement with the 2D scattering model. We have designed, fabricated and characterized straight waveguides, S-bends and Y-splitters that work under these conditions. The structures feature different characteristics and performance variations for the different channel widths in the wavelength range 740–840 nm. The straight waveguides exhibit propagation lengths of $> 10 \ \mu$m for the case of 2-μm-wide channel. The S-bends and Y-splitters also show efficient guiding and bending of the RN-PCW modes. We believe that it is possible to further improve their performance by optimizing the nanoparticle size and density. These results open the possibility for designing the next generation of the RN-PCW-based components, based on the scattering parameters that we established in this work, so as to explore other waveguide configurations for plasmonic circuitry.

Acknowledgments